Hindawi
International Journal of Aerospace Engineering
Volume 2019, Article ID 7982168, 21 pages
https://doi.org/10.1155/2019/7982168

Research Article

Aerodynamic Shape Design and Validation of an Advanced High-Lift Device for a Regional Aircraft with Morphing Droop Nose

Alessandro De Gaspari[1] **and Frédéric Moens**[2]

[1]*Department of Aerospace Science and Technology, Politecnico di Milano, 20156 Milano, Italy*
[2]*Aerodynamics Aeroelasticity and Acoustics Department, ONERA, The French Aerospace Lab, 92190 Meudon, France*

Correspondence should be addressed to Alessandro De Gaspari; alessandro.degaspari@polimi.it

Received 15 April 2018; Accepted 4 December 2018; Published 27 March 2019

Academic Editor: Mauro Pontani

In the present work, the aerodynamic shape design of an advanced high-lift system for a natural laminar flow (NLF) wing, based on the combination of a morphing droop nose and a single slot trailing edge flap, is presented. The paper presents both the aerodynamic design and optimization of the NLF wing and the high-lift configuration considering the mutual effects of both flap devices. Concerning the morphing droop nose (DN), after defining the parameterization techniques adopted to describe the geometry in terms of morphing shape and flap settings, the external configuration is obtained by an aerodynamic shape optimization procedure able to meet geometrical constraints and the skin structural requirements due to the morphing. The final performance assessment of the three-dimensional high-lift configurations is performed by high-fidelity aerodynamic analyses. The design procedure is applied to a twin-prop regional aircraft equipped with a natural laminar flow wing. The morphing droop nose is compatible with an NLF wing that requires the continuity of the skin and, at the same time, extends the possibilities to improve the performances of the class of regional aircraft which usually are not equipped with conventional leading edge devices. Additionally, the morphing technology applied to the flap allows the design of a tracking system fully integrated inside the airfoil geometry, leading to a solution without external fairings and so with no extra friction drag penalty for the aircraft.

1. Introduction

In the field of the innovative high-lift device technologies, the active camber morphing represents an interesting concept, due to its capabilities to improve the aerodynamic performances and to redefine the takeoff and landing maneuvers configurations, offering the possibility to be immediately installed on the existing wing without the need to replace the structural wing box. One of the main devices that allow changing the wing camber is the morphing droop nose. Many applications of this concept are described by Friswell in [1]. Around 1973, Boeing performed a wind tunnel test comparison on a wing equipped with hinged leading and trailing-edge flaps, and then with smooth variable-camber flaps that provided large improvements [2]. More than ten years later, Boeing started several research programs aimed at embedding active camber devices on board a military aircraft [3–5]. In the Advanced Fighter Technology Integration (AFTI) program, by NASA and USAF, the F-111 wing was equipped with control surfaces, driven by electrohydraulic actuators, based on sliding panels for the lower trailing edge, and composite flexible panels for the upper trailing edge and for the leading edge. The AFTI/F-111 flight tests confirmed a performance increase of 20% in terms of aerodynamic efficiency and 15% in terms of distributed load on the wing, keeping constant the bending moment [6, 7].

One of the most important contributions to the design of morphing droop nose comes from Monner, who developed different concepts during the years. At the beginning, he tried to replace the leading edge ribs with several plates, fitting into

the airfoil shape, and connected each other with rigid hinges, whereas the skin is free to slide along the airfoil contour by means of joint and stringers that restore the required stiffness [8, 9]. The rib elements were optimized to minimize the hinge stress. Afterwards, Monner continued his collaboration with EADS, within the SmartLED project, to realize a patent smart leading edge device to be used in a typical high-lift application and to replace the droop nose installed on the A380. This morphing droop nose was optimized to reach a deflection of 20 deg, keeping smooth the external surface. Recently, different EU projects, such as SADE and SARISTU, started from Monner's work to design a portion of a full-scale morphing droop nose composed of two main parts: a compliant skin and a rigid kinematic mechanism obtained by an integrate design [10]. Other projects also concerned the development of morphing flap [11, 12] and morphing trailing edge [13, 14] devices for the load control in both high-speed and low-speed conditions.

Nowadays, one of the most technologically advanced companies in the field of adaptable shape structures is FlexSys Inc. which developed specific tools for the design of devices based on the compliant structure concept. They cover different fields of application, including morphing wing equipped with seamless and hingeless leading and trailing edge devices, without any rigid mechanism [15, 16]. They are strongly focused on obtaining completely continuous and smooth surfaces able to optimize the aerodynamic efficiency in different flight conditions. A compliant flap system was designed to maximize the laminar boundary layer over a wide lift coefficient range by continuously optimizing the shape throughout the mission. This technology was successfully installed on the NASA Gulfstream aircraft by replacing the original flap.

The work presented in this manuscript starts in the framework of EU-funded Clean Sky 2 REG-IADP AG2 project, where innovative high-lift device technologies, able to achieve new design requirements and suitable to be applied to the natural laminar flow (NLF) wing of a Green Regional Aircraft, have been investigated. In a first step, the wing shape of the reference Green Regional Aircraft has been redesigned to obtain a large portion of natural laminar flow on both surfaces at cruise and off-design flight conditions. The aircraft configuration equipped with this new NLF wing has been used as baseline for the design of innovative high-lift devices to be considered at takeoff and landing conditions.

A morphing droop nose installed on the wing of an existing Regional Aircraft provides significant aerodynamic benefits because this kind of medium-size civil aircraft are usually not equipped with conventional leading edge devices. Moreover, the morphing droop nose allows redesigning the baseline wing shape that can be optimized considering only the flight conditions that do not require the shape changes introduced by the morphing. This second aspect provides an additional advantage in terms of aerodynamic benefit because different external shapes can be defined to optimize the aerodynamic performances in different flight conditions. The different shapes can be designed separately considering that the morphing allows the transition between them, preserves the shape continuity, and avoids any type of step and gap. This advantage is greater in the case of the laminar wing where the NLF wing can be optimized for the high-speed conditions and the same wing, equipped with the morphing droop nose, for low-speed conditions.

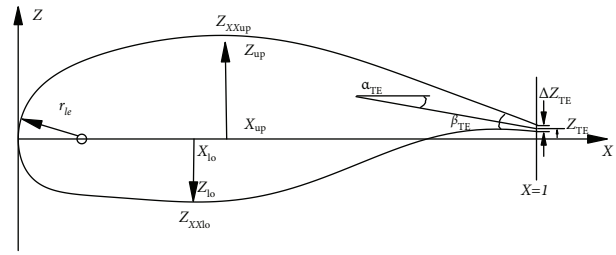

Figure 1: Airfoil parameterization used for numerical optimization (PARSEC).

Starting from the studies carried out during the participation to previous EU projects, such as SARISTU and NOVEMOR [17, 18], the optimal morphing droop nose has been designed to be installed on the Green Regional Aircraft, in terms of both external morphing shape and internal compliant mechanism [19, 20]. In this manuscript, only the dedicated shape optimization process, adopted for the aerodynamic shape design of the complete high-lift device, is described starting from the "clean" NLF wing geometry. In order to obtain the maximum benefit in both high-speed and low-speed conditions, the NLF wing geometry was defined before, considering the cruise condition, by a shape optimization based on the geometry parameterization from PARSEC [21]. Afterwards, the morphing droop nose shape was obtained by a second optimization procedure, based on the CST (class-shape transformation) parametric technique [22, 23], extended to the description of 3D shapes for this work. The complete optimization procedure, including the designing of the flap system, has been applied to the Green Regional Aircraft inside the Clean Sky 2 REG-IADP AG2 project.

This paper summarizes the results obtained during this work and is organized in three main parts: the optimization of the NLF wing, followed by the flap system design; the morphing droop nose shape optimization; and the performance assessment at the aircraft level in high-lift configurations by advanced chimera techniques and aerodynamic computations.

2. Design of the Regional Aircraft NLF Wing

The initial Green Regional Aircraft wing has been redesigned in order to have an extended natural laminar flow on the upper and lower surfaces in cruise conditions, by an optimization process based on the PARSEC airfoil geometry representation [21]. The parameterization method uses the 11 design variables shown in Figure 1, whereas the adopted optimizer is the DOT gradient-based method from Vanderplaats [24] that works to minimize an objective function defined as the sum of drag coefficients at different C_L values in high-speed condition, under some constraints on the original

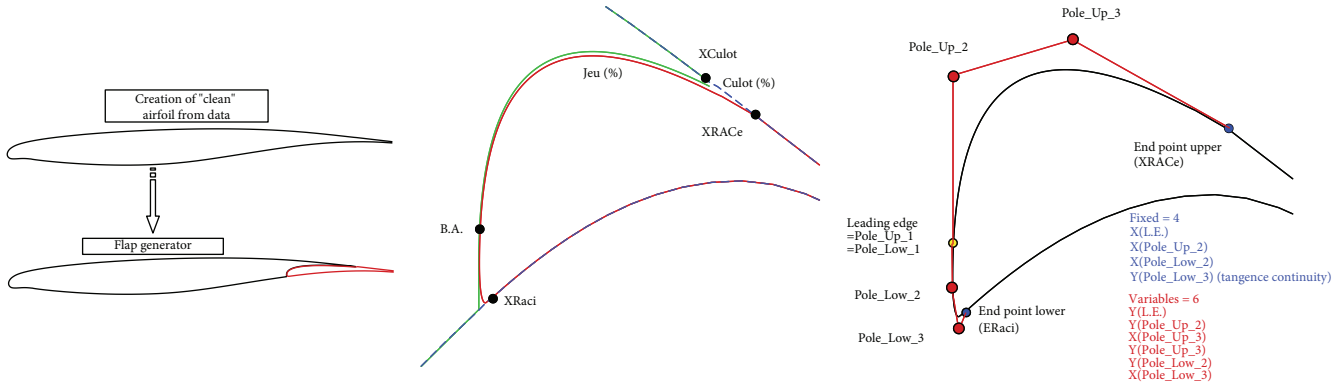

(a) Principle (b) Design constraints (c) Curve parameterization

Figure 2: Flap shape generator used at ONERA.

wing structure sizing and fuel tank capacity. To have the possibility to evaluate many airfoils in a reduced time frame, fast CFD methods are used in the optimization process, namely, Drela and Giles' ISES/MSES code [25].

Once the shape of the NLF wing is defined, it can be used to introduce the shape changes due to the morphing only in high-lift conditions, together with the configuration changes due to the flap deployment. Previous works in the scientific literature show that the aerodynamic evaluation of a morphing droop nose, optimized for low-speed conditions, must be performed considering the wing in its high-lift configuration [18]. For this reason, the shape design of the flap is performed before. An ONERA in-house shape generator has been used for 2D flap design. The principle is to start from the clean airfoil, then to generate the flap shape and finally to set it at a given location according to desired gap/overlap and deflection. Concerning the requirements related to steps and gaps, the effects are important around the cruise because they can trigger transition, so you lose the laminar flow. Specific criteria to identify the maximum dimensions of steps and gaps acceptable to avoid this problem are addressed at this stage and evaluated by RANS computations. This subprocedure for the design of the flap system is reported in Figure 2.

The shape generator is based on a set of Bezier curves for upper and lower parts of the flap and respects some geometrical constraints. It has been used in previous activities dealing with numerical optimization of high-lift systems [26]. Due to the limited time frame for the delivery of a high-lift system for the AG2-NLF plane, a design phase has been preferred to a pure optimization.

2.1. Aerodynamic Solvers and Grid Generation. The CFD solver used in this study is the elsA solver [27, 28]. The elsA software (ONERA-Airbus-Safran property) solves the compressible three-dimensional RANS equations by using a cell-centered finite volume spatial discretization on structured multiblock meshes. For the spatial scheme, the one proposed by Jameson et al. [29] is used for the conservative variables. A fourth-order linear dissipation k_4 is generally used, with added second-order dissipation terms k_2 for treatment of flow discontinuities. In the present study, k_2 was set to zero due to the low free stream Mach number, and the fourth-order dissipation was set to $k_4 = 1/16$ or 1/32. The turbulence model used is either the one equation Spalart-Allmaras model with the QCR modification [30] for computations at cruise conditions or the two-equation $k - \omega$ Menter SST one [31] for computations of high-lift configurations. For the implicit stage, a LUssor scheme is associated with an Euler backward time integration scheme, which allows fast convergence rates. For the turbulent variables, an extension to the second order of the Roe numerical scheme is used with a Harten entropic correction coefficient set to 0.01 and the "minmod" limiter. Finally, multigrid computations and low-speed preconditioning have been used for convergence acceleration.

For the performance evaluation of the NLF wing at cruise conditions, it is necessary to compute the location of the transition line on the wing. During the RANS computations, the elsA software has the capability to compute laminar flow regions and to determine the transition location by using the so-called AHD compressible criterion for Tollmien-Schlichting instabilities [32] and the so-called C1 criterion for crossflow instabilities [33], within the iterative convergence process as described in [34].

The meshes used for the aerodynamic computations have been generated with the ICEM-CFD commercial software [35]. In order to deal with the geometrical complexity of the aircraft configuration with high-lift devices deployed, the use of chimera overset grids has been considered, as it considers only a first set of grids to be generated (for the main element and for the flap) and settings modification is then taken into account by simple displacement of the flap grid. This technique has been used for both two-dimensional computations, for preliminary concept selections, or three-dimensional cases for aircraft performance evaluation.

The chimera preprocessing has been done using the chimera capabilities of the elsA software for 2D configurations or the ONERA Cassiopée suite [36] for 3D configurations. An example of this preprocessing is presented in Figure 3 for a 2D application.

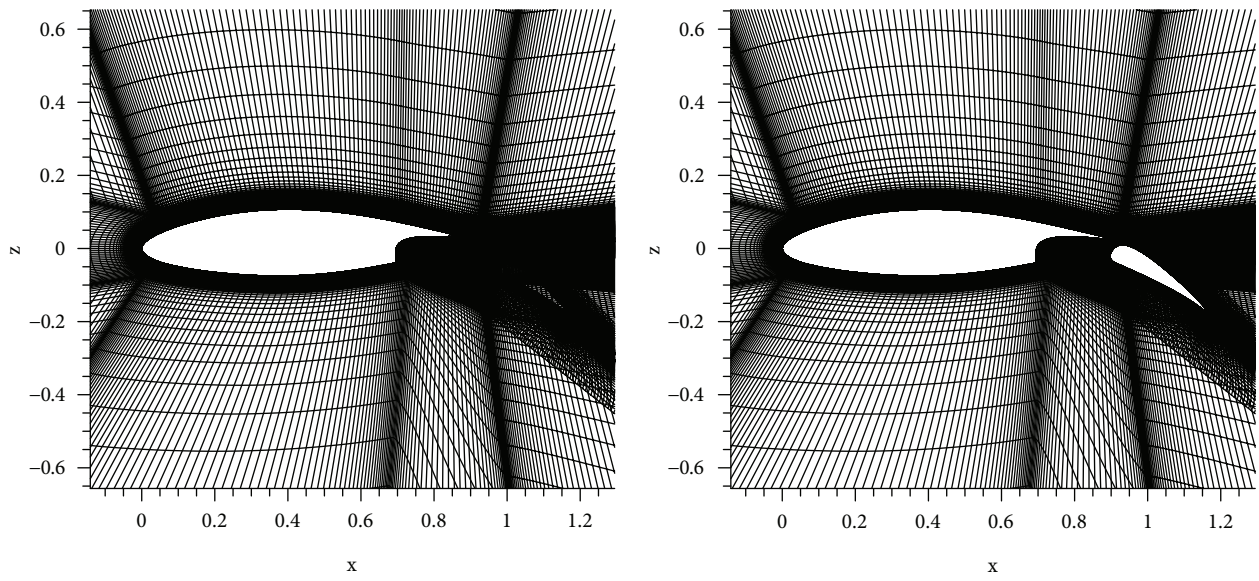

(a) Original grids

(b) After chimera preprocessing: masked cells are blanked

Figure 3: Example of chimera grids used for 2D.

Table 1: Flight conditions considered for NLF wing design.

	Mach number	Altitude (ft)	Reynolds (10^6)	C_L (wing + body)
Cruise (1)	0.52	20 000	17.33	0.50
Climb (2)	0.45	20 000	15.00	0.67
Low speed (3)	0.197	0	11.80	

Table 2: Range in local C_L coefficients considered for the airfoil multipoint optimization.

	Lower bounds	Design	Upper bounds
Root airfoil	$C_L = 0.25$	$C_L = 0.50$	$C_L = 0.90$
Tip airfoil	$C_L = 0.10$	$C_L = 0.30$	$C_L = 0.60$

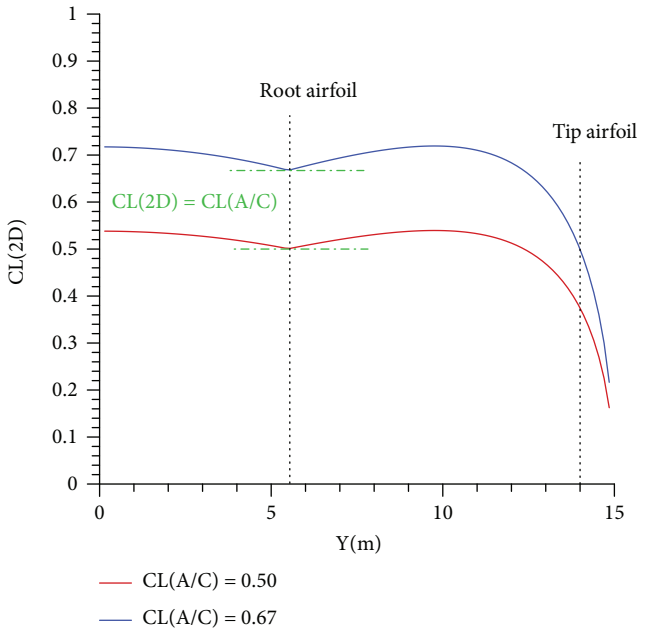

Figure 4: Spanwise evolution of the local lift coefficient for flight conditions 1 and 2.

2.2. Natural Laminar Flow Wing. The reference aircraft considered in this project is a 90-pax configuration. For the Green Regional Aircraft project, the wing was redesigned at cruise conditions, but the wing planform was not modified. The design considered a multipoint optimization of the tip and root airfoils for cruise, climb, and low-speed conditions (Table 1), in order to have a satisfactory performance level on a large part of the flight domain.

During the optimizations carried out for this study, only the PARSEC variable related to the trailing-edge thickness ΔZ_{TE} is fixed, and so, the numerical optimization process considers 10 design variables. Note that the PARSEC parameterization does not use the absolute value of the maximum thickness and that maximum thickness is not equal to $Z_{XXup} - Z_{XXlo}$ (true only if $X_{up} = X_{lo}$). Therefore, for each airfoil considered during the optimization process, its maximum thickness is calculated and compared to the required values through an inequality constraint. Similar treatment is made for checking the relative thicknesses at front or rear spars.

As we consider 2D optimizations, the C_L level considered for the design point has to correspond to local values observed on the wing at airfoil location. A tool used for preliminary conceptual design, based on analytical relations, has been used in order to make this correlation (Figure 4). It can

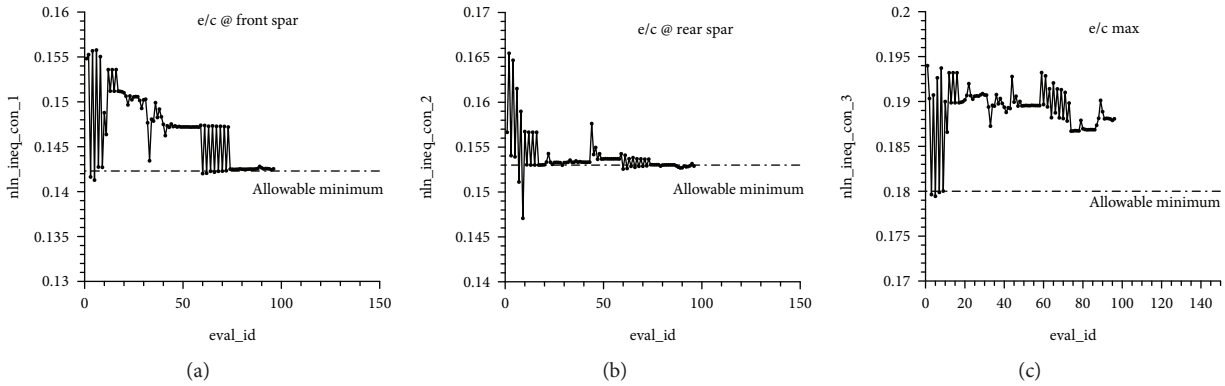

Figure 5: Evolution of the different thicknesses during the optimization process for root airfoil.

Table 3: NLF-optimized airfoils – relative thicknesses at given locations.

NLF airfoils	Root airfoil	Tip airfoil
Maximum thickness	18.8%	13.7%
Thickness at $X/C = 16\%$	14.25%	10.85%
Thickness at $X/C = 60\%$	15.30%	10.60%

be seen that for the root airfoil, the local C_L to be considered is in the same order of magnitude than the aircraft lift coefficient (green curves), whereas for the tip airfoil, the 2D values correspond to about 50% of the 3D ones.

In a practical point of view, due to the low difference in Reynolds numbers between flight conditions 1 (cruise) and 2 (climb), the airfoil design process considered only the flight condition 1 (cruise) as aerodynamic conditions. The effect of climb conditions on the airfoil design was obtained by considering the corresponding C_L values in the composite cost function. Therefore, the ranges in C_L reported in Table 2 have been retained for the airfoils design.

The objective function to be minimized by the DOT gradient-based optimizer is the sum of drag coefficients at different C_L values. In order to respect some constraints on wing structure sizing and fuel tank capacity, the different minimum thickness values (for $(e/c)_{max}$ and e/c at spars) have been considered as constraints in the optimization process. It is interesting to note that the trend of the optimization process is to obtain an airfoil that respects the constraints at the front and rear spars, but the resulting maximum thickness is slightly higher than the reference one, for both the root and the tip airfoils. Figure 5 presents the evolution of the different constraints during the optimization process on airfoil thickness for the root airfoil. This is due to the fact that the design tends to generate a shape with a favorable pressure gradient for NLF flow which is constrained by the thicknesses at spar location.

At the end of the optimization process, the airfoils have been rescaled in order to strictly respect the constraints at front and rear spars. Table 3 presents the final values for relative thicknesses at given locations for the two baseline airfoils.

Figure 6 compares the computed aerodynamic performance of the airfoil of the reference plane at the root with the ones of the optimized airfoil with extended NLF characteristics. Similar comparisons for tip airfoils are presented in Figure 7. It has to be noted that the airfoils extracted from the reference plane present some NLF characteristics, but at too high C_L values for the tip airfoil.

For root airfoils (Figure 6), the NLF performance of the optimized airfoil has been extended over a large range of C_L, even though the minimum drag coefficient could not be improved. However, it can be noted that in fully turbulent flow conditions, the aerodynamic performance of the optimized NLF airfoil is improved compared to the reference airfoil.

For tip airfoils (Figure 7), the NLF performance of the optimized airfoil has been extended over a large range of C_L, particularly in the domain of low C_L values. In turbulent flow conditions, the performances of the optimized NLF airfoil and of the reference airfoil are comparable.

In a second step, a NLF wing has been obtained by considering the two NLF airfoils designed previously, the same planform as the reference wing one, and including sweep and dihedral. The twist of the outer part of the wing has been optimized in order to shift the stall onset outside the aileron area at flow conditions 3 (low speed). A linear twist of 4° between the kink and the tip has been obtained. For the untwisted wing, a nearly elliptical span loading was achieved (Figure 8). The application of a linear twist on the outer wing leads to a nearly linear variation of the span load, which will imply a degradation of the lift-induced drag component through the Oswald factor.

This final optimized wing has been then adapted to the reference aircraft configuration, leading to the so-called AG2-NLF aircraft configuration. This work considered the design of new Karman between the wing and the fuselage, and the adaptation of a reference winglet at the wing tip (see Figure 9).

The evolution of the computed transition locations on the wing, with the elsA software (SA-QCR model) when the

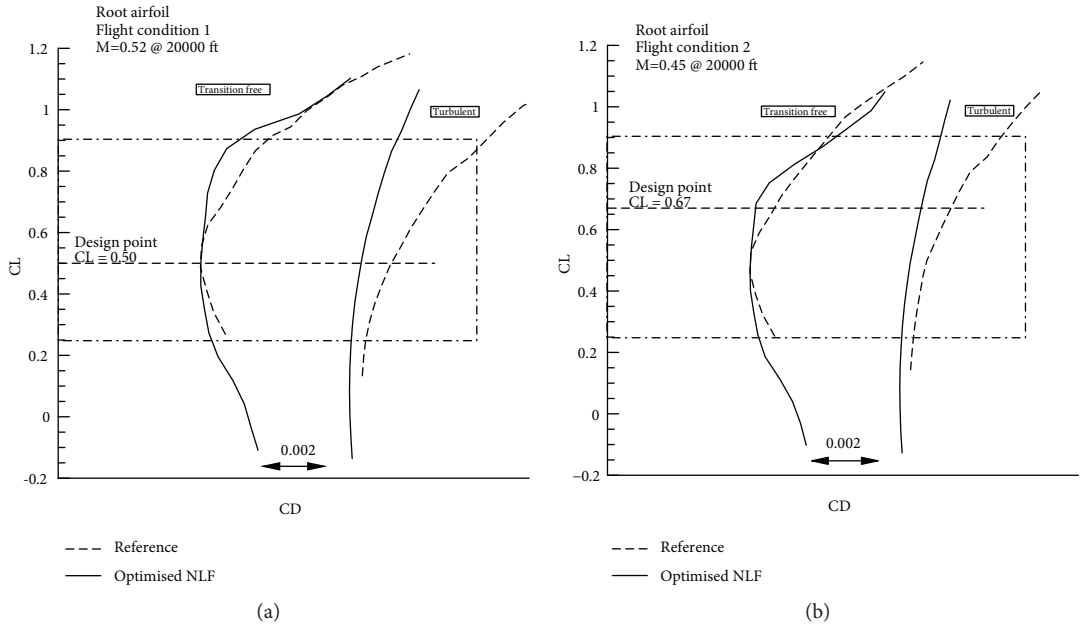

Figure 6: Computed 2D performance of optimized root airfoil.

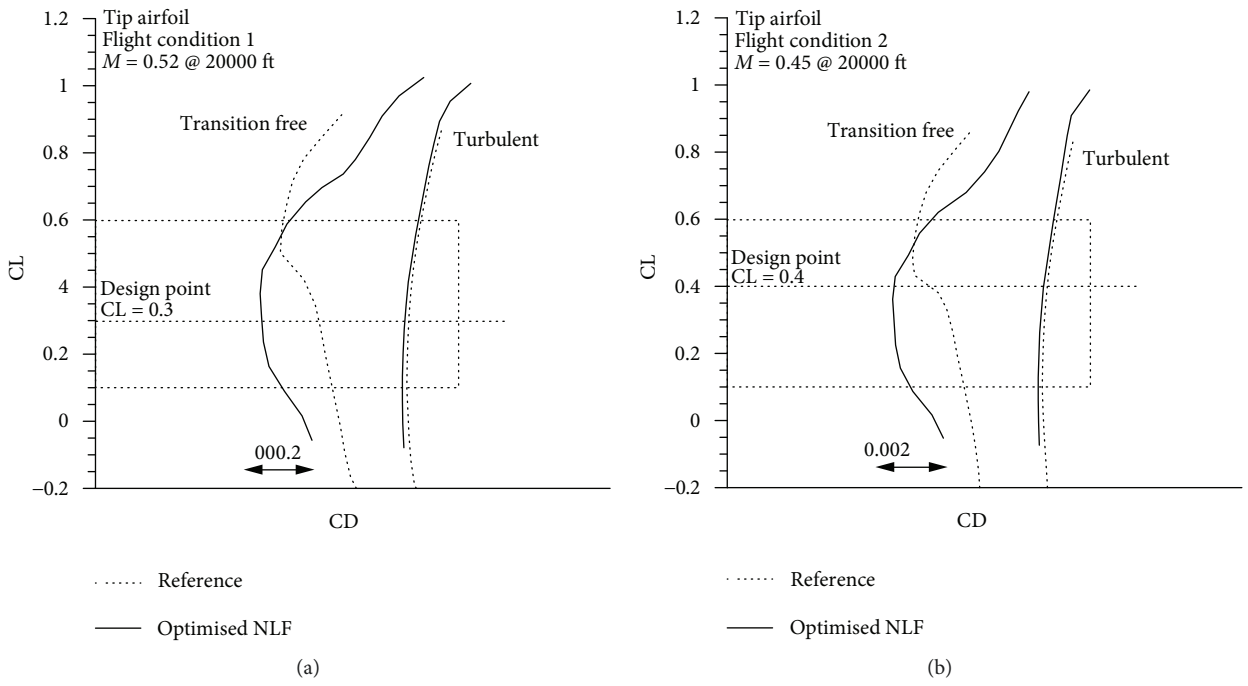

Figure 7: Computed 2D performance of optimized tip airfoil.

angle of attack increases, is presented in Figure 10 for the upper surface and in Figure 11 for the lower surface. In these figures, the wind direction is from left to right.

The different design integrations made do not significantly affect the NLF characteristics of the wing. On a general overview, there is a laminar flow extension on about 50% of both surfaces on a large range of incidence. On the upper surface, natural laminar flow is lost for α higher than 6.5° roughly. On the lower surface, at $\alpha = 0°$, the wing tip area is turbulent, but the other regions have a laminar flow extension nearly up to mid-chord.

In terms of performance, the NLF technology allows a global drag reduction by about 40 drag counts at the flight C_L condition when comparing with fully turbulent results.

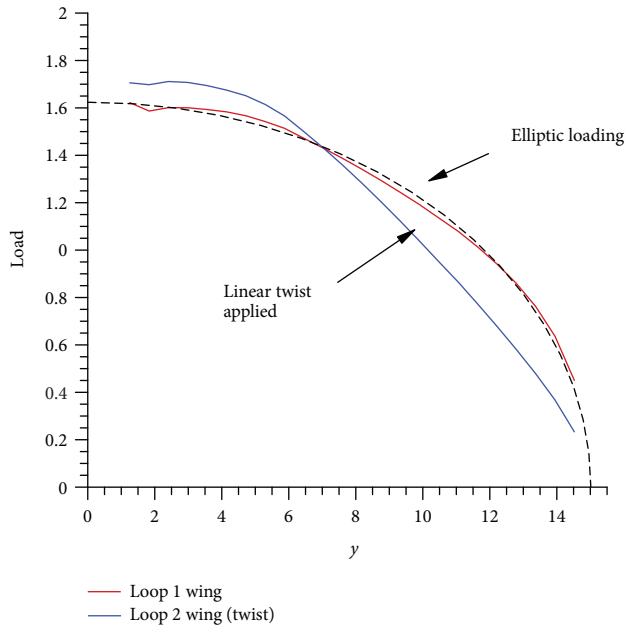

Figure 8: Effect of twist on the span loading distribution at cruise conditions (M = 0.52 @ 20000 ft, CL = 0.50).

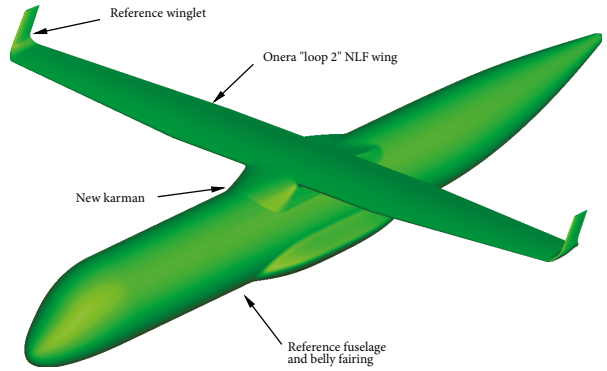

Figure 9: AG2-NLF configuration considered.

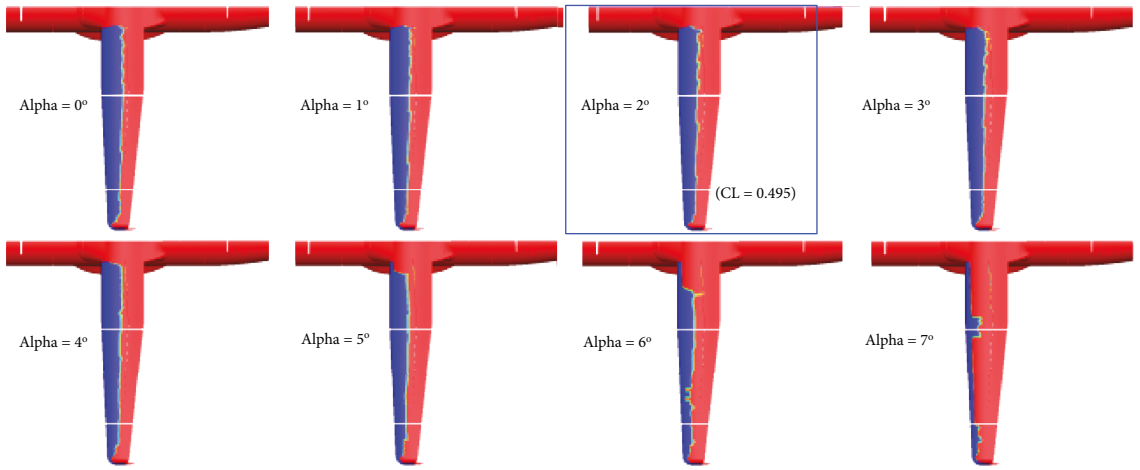

Figure 10: AG2-NLF plane: computed transition location on the wing upper surface at cruise conditions (M = 0.52 @ 20000 ft). Blue = laminar, red = turbulent.

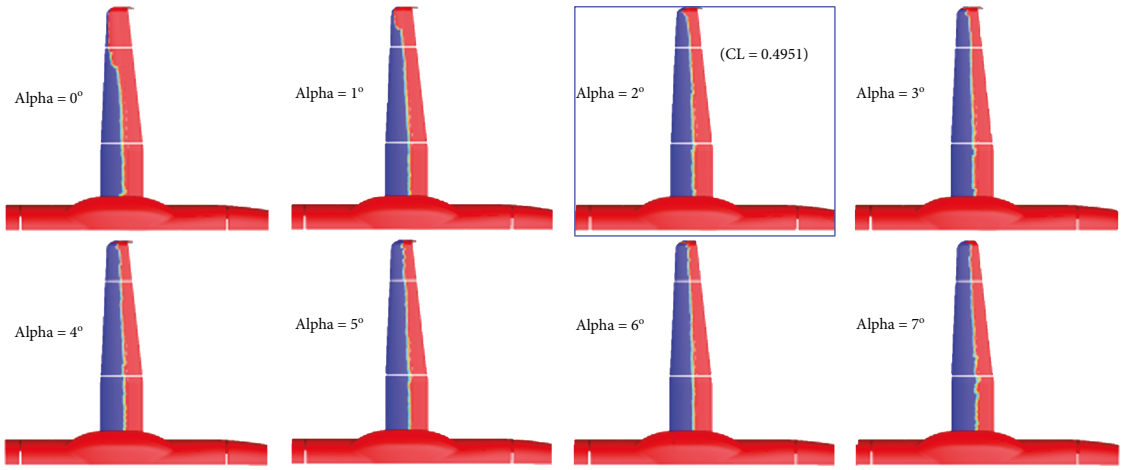

Figure 11: AG2-NLF plane: computed transition location on the wing lower surface at cruise conditions (M = 0.52 @ 20000 ft). Blue = laminar, red = turbulent.

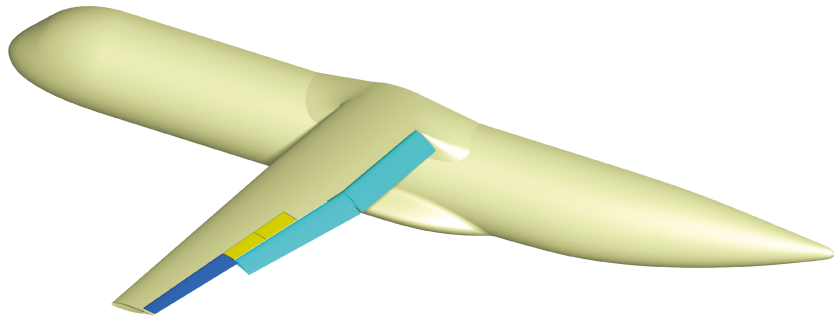

Figure 12: General layout of the AG2-NLF wing for flap arrangements.

Table 4: Geometrical constraints used for flap design.

Shroud (upper surface)	$X/C = 0.9250$
Cove (lower surface)	$X/C = 0.6950$
Main wing TE thickness	$e/c = 0.15\%$
Gap between flap and wing	$g/c = 0\%$

2.3. Flap System. Figure 12 presents a general view of the flap arrangements on the AG2 wing. The wing can be divided into two main parts:

(i) A rectangular inboard part, from the symmetry plane to a kink section

(ii) A trapezoidal outboard part, from the kink to the wing tip

According to the baseline airfoil definition for the clean wing, the shape definition process of the flap considered two sections:

(i) One located in the outboard part, with local performance representative of the aircraft level

(ii) One located in the root/inboard part, in order to generate the flap 3D shape

Table 4 presents the geometrical constraints considered for the design of the flap system, derived from industrial requirements and from the reference turbulent aircraft. The final shape and its corresponding settings for takeoff (with a flap deflection of 20°) and landing (for a flap deflection of 35°) for the outboard wing section is presented in Figure 13. Similar work has been carried out for the inboard wing section, in order to generate three-dimensional flap geometry.

The gap between flap and wing in stowed position has been set to zero as the initial gap (0.53%) seemed quite large for morphing control in high speed, considered in another task of the project, without any significant penalty in drag.

The characteristics of the grids used in the 2D computations (for one plane) are shown in Table 5.

The computed aerodynamic performance of the takeoff and landing configurations obtained are presented in Figure 14: the dashed lines correspond to an estimation of the performance level to be reached at the outboard wing section, derived from the 3D aerodynamic performance required. It can be seen that the two configurations designed reach the requested performance level but with no margin. In addition, a high-pressure peak is observed

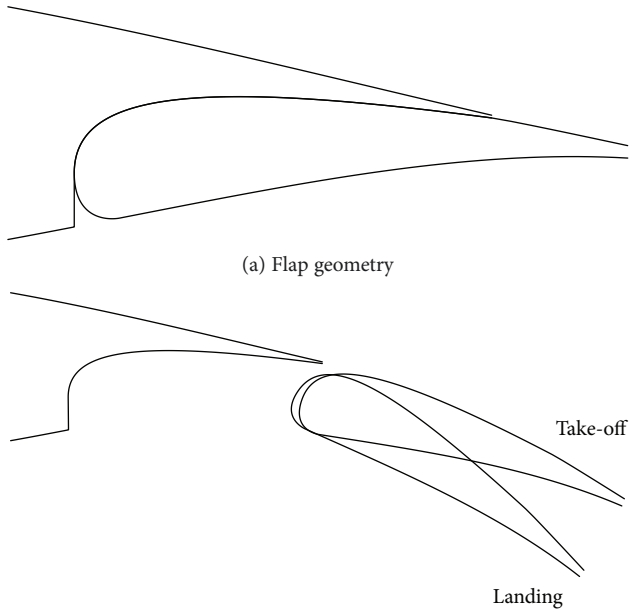

Figure 13: Outboard flap.

Table 5: Grid dimensions for the 2D CFD performance evaluation using chimera technique.

Background/main airfoil	123,377 nodes
Flap	17,936 nodes
Total	141,313 nodes

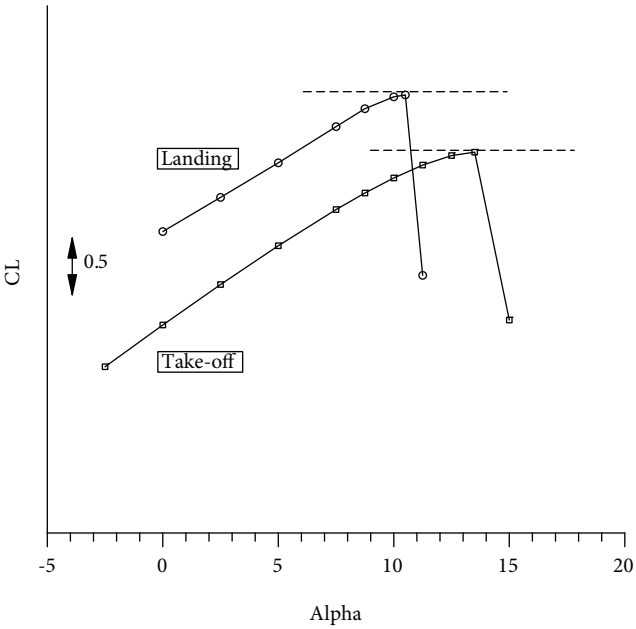

Figure 14: Computed aerodynamic performance of takeoff and landing configurations for the outboard wing section without the droop nose device (2D).

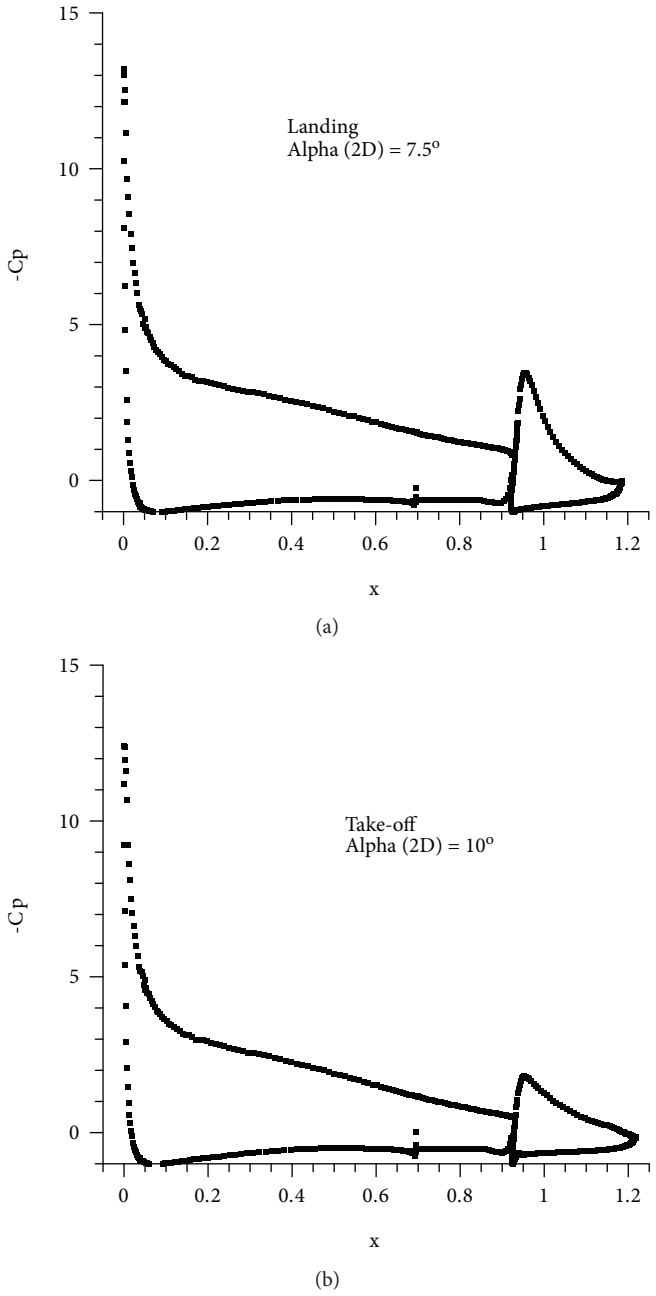

Figure 15: Computed pressure coefficients at high angle of attack without droop nose device.

Table 6: Flap setting for the high-lift conditions.

Final settings	LDG	TO
Deflection	35 deg	20 deg
Gap/chord	2.16%	2.26%
Overlap/chord	-0.25%	-0.43%

at the wing leading edge (Figure 15). This high-pressure peak is characteristic of high-lift configuration with no leading edge devices, but is amplified in this case due to the NLF design of the wing.

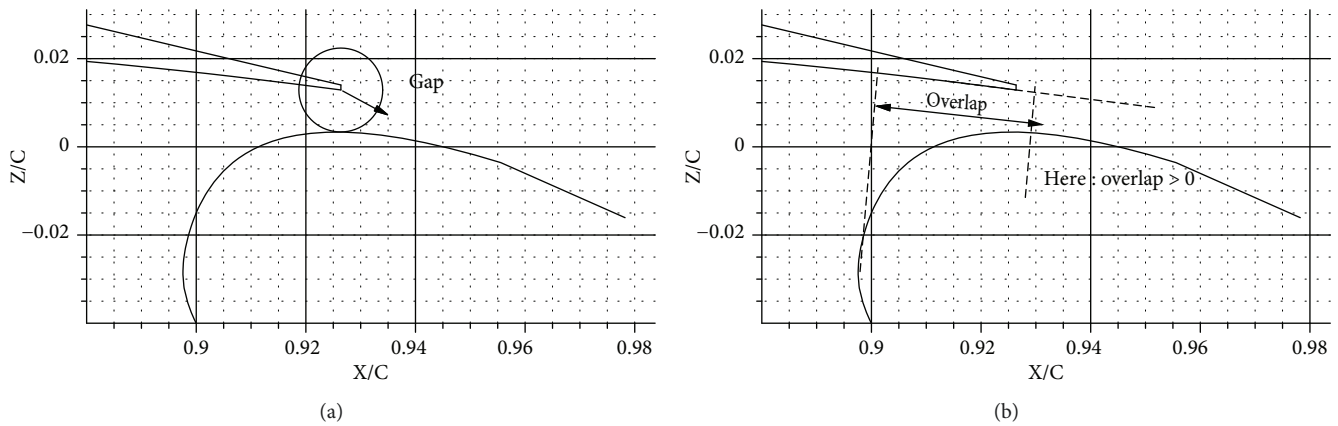

Figure 16: Definition of gap and overlap used for flap settings.

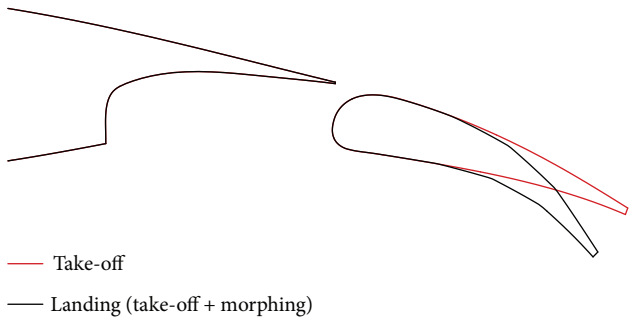

Figure 17: Flap system retained for landing configuration on the AG2-NLF aircraft.

An improvement of high-lift performance for both $C_{L\,\max}$ and stall angle can be obtained by the use of a leading edge device only. Among the different mechanical devices compatible with keeping the extended laminar flow on the wing at cruise, the droop nose is the best candidate.

The final settings of the flap system is given in Table 6, according to the gap and overlap definitions presented in Figure 16.

A final design step has been considered due to a specific requirement at aircraft level. It was asked to propose solutions for high-lift systems that minimize the impact on aircraft performance at cruise conditions. Therefore, the actuation tracks should be the simplest possible so to be hosted into the wing airfoil shape without external fairings. When considering the optimized settings for the designed flap, it was found that such constraint was possible for takeoff or landing, but not for both. To meet this requirement, a strategy considering morphing technology on the flap has been retained. The best strategy found considers first to move the flap at its takeoff settings. In that case, a solution without external fairing is possible. Then, morphing is applied to the flap shape for landing conditions as illustrated in Figure 17.

3. Droop Nose Morphing Shape Optimization

Once the NLF wing shape and the flap configuration are defined, the morphing droop nose is designed by a dedicated shape optimization able to combine the minimization of the aerodynamic drag coefficient in high-lift conditions and the maximization of the leading edge deflection, under structural constraints to limit bending and axial stresses inside the skin when the morphing shape changes are introduced. According to the methodology already presented in [22, 23], this optimization procedure is based on a parametric CST representation of the geometry, significantly improved in this work to provide three-dimensional capabilities. Depending on the nature of the problem, different optimization processes can be implemented, combining the geometry parametric representation, the prediction of the skin structural response, and the aerodynamic solver. Two main architectures can be defined.

The integrated approach, where both structural and aerodynamic evaluations are considered at the same time during the optimization, is shown in Figure 18. This scheme is strictly related to the 3D CST representation described in the next section. The morphing shape is computed, during each optimization step, to implicitly satisfy the wing box constraint in the undeformed region and the required spanwise deflection law in the morphing region of the 3D wing. However, the aerodynamic evaluation can be performed on morphing shapes that do not meet the structural constraints in terms of strain along the skin. This approach is penalizing when the problem is dominated by the skin structural constraint, such as in the case of this study where the goal is to find the maximum droop nose deflection for the high-lift conditions.

For this reason, a second shape optimization scheme, where the set of the most characteristic cross sections are combined to define the optimal morphing shape after the structural constraints are satisfied, is adopted in this work. This hybrid approach consists of two nested optimization loops: the inner one is a structural optimization where the objective function is based only on geometric considerations, related to the CST parameters, while the outer one works only on feasible shapes used for the aerodynamic evaluation. Moreover, when the aerodynamic computation must be performed in low-speed conditions and the geometry includes the deployed flap, 2D aerodynamic analyses are considered and the same CFD method used for the NLF wing optimization (Drela and Giles' ISES/MSES code [25]) is embedded with the optimization process.

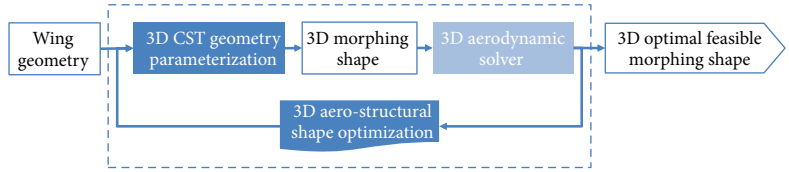

Figure 18: Aerostructural shape design: integrated approach.

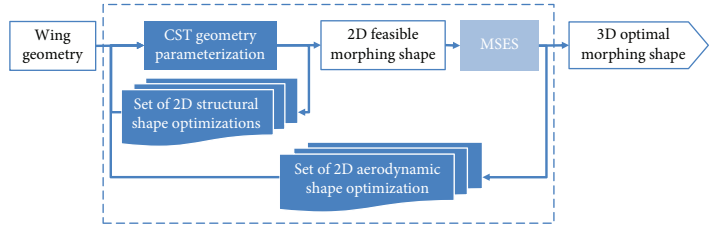

Figure 19: Aerostructural shape design: hybrid approach for high-lift configurations.

The hybrid approach, applied to the study presented in this paper, is shown in Figure 19. The inner loop includes the structural considerations in terms of structural response of the skin. In this way, only morphing shape changes that meet preassigned structural requirements are considered during the aerodynamic computation. Morphing shape changes are introduced only through the airfoils in the set of the most characteristic cross sections. After the set of the corresponding morphing airfoils is optimized, the 3D parameterization technique allows to meet the 3D constraints, related to the undeformed wing box and to the spanwise deflection law, in the region between the considered cross sections.

Starting from the NLF wing geometry, optimized for the cruise condition and based on the PARSEC parameters, the corresponding CST model is generated by the 3D parameterization techniques described in the next section. The output of this step is one shape object, in the object-oriented programming (OOP) sense, related to a common 3D shape representation of the initial wing geometry. The geometry modifications due to the morphing are introduced by the CST parametric capabilities and spread over all the steps performed inside the optimization procedure. Additional required input are the material properties, such as the equivalent Young's modulus E and the minimum skin thickness t to be assigned to the morphing skin. The output of the shape optimization is the shape object related to the morphing shape.

The optimization variables are potentially all the geometric parameters embedded into the 3D CST formulation. However, for the hybrid approach of Figure 19, the set of CST parameters, used to represent the set of the most characteristic cross sections, is split in two subsets, one for the inner loop and one for the outer loop: the optimization variables used in the inner loop are selected to make the procedure capable to satisfy the skin structural requirements; the optimization variables used in the outer loop are selected to provide the control over the aerodynamic performances. Constraints related to the wing box volume and to the spanwise deflection law are applied outside the outer loop combining the optimal morphing airfoils by the spanwise Bernstein polynomials adopted in the 3D CST parameterization.

3.1. 3D Parametric Representation. The CST representation of the actual 3D wing geometry can be described by

$$z(x, y) = \zeta(\psi, \eta) \cdot c(\eta), \tag{1}$$

where $x = \psi \cdot c(\eta) + x_{\mathrm{LE}}(\eta)$, $y = \eta \cdot b/2$ are the dimensional coordinates defined with respect to the wing span b and to the distribution of the local chord $c(\eta)$ and the horizontal leading edge position $x_{\mathrm{LE}}(\eta)$ in spanwise direction. The upper and lower nondimensional surfaces are

$$\zeta(\psi, \eta) = C_{N2}^{N1}(\psi) S(\psi, \eta) + \psi \zeta_{\mathrm{TE}}(\eta) + (1 - \psi)\zeta_{\mathrm{LE}}(\eta), \tag{2}$$

where $\zeta_{\mathrm{LE}} = Z_{\mathrm{LE}}/c$ and $\zeta_{\mathrm{TE}} = Z_{\mathrm{TE}}/c$ are the nondimensional vertical leading and trailing edge position. The class function $C_{N2}^{N1}(\psi)$ has already been defined in [22], whereas the shape function $S(\psi, \eta)$ represents a 3D surface and can be described by the 2D matrix:

$$\mathbf{P}_{2D} = \mathbf{Sy}_{m,m} \cdot \mathbf{A}_{m,n} \cdot \mathbf{Sx}_{n,n}. \tag{3}$$

The polynomial coefficients $\mathbf{P}_{2D}$ in descending powers can be computed as a scalar product of the square matrix **Sy** containing the coefficients of the unit spanwise shape function for the Bernstein polynomial of order m; the rectangular matrix $\mathbf{A}_{m,n}$ containing the extra-coefficients acting in spanwise and chordwise directions, respectively; and the square matrix **Sx** containing the coefficients of the unit chordwise shape function for the Bernstein polynomial of order n. Each row of the matrix $\mathbf{A}_{m,n}$ defines a component airfoil, according to [37], and the first and last rows contain the extra-coefficients of the two airfoils placed at the spanwise boundaries of the wing. The first and last columns of the matrix $\mathbf{A}_{m,n}$ are

related to the leading and trailing edge boundary conditions and can be used to satisfy the spanwise deflection law constraints. All the other coefficients of the matrix $\mathbf{A}_{m,n}$ can be the optimization variable. However, if only the morphing leading or trailing edge shape must be optimized, the matrix can be partitioned into two submatrices: the portion of extra-coefficients acting on the morphing region contains the optimization variables, and the other extra-coefficients can be evaluated by a closed-form least-squares fitting able to meet the constraint related to the 3D wing box volume.

Once the CST representation of a 3D wing is available, morphing shape changes can be introduced. A list of coordinates $(x(nal), y(nal))$ can be used to define the inverse of the normalized arc length function that identifies a path on the 3D surface. The length L and the curvature κ variations, between the undeformed and the morphing shapes, computed along the same path are strictly related to the bending and axial stresses generated when the skin is forced to assume the morphing shape. The bending stress is computed in the same way, calculating the curvature difference between the initial and final wing shapes, with respect to the same normalized arc lengths *nal*, as follows:

$$\Delta\kappa(nal) = \kappa_m(x(nal), y(nal)) - \kappa_u(x(nal), y(nal)), \quad (4)$$

where κ_u and κ_m are the curvature functions of the undeformed and morphing wings. The length variation of the morphing skin ΔL_{dev} with respect to the undeformed one $\Delta L_{\text{dev},u}$ can be related to the skin of a leading edge device $\Delta L_{\text{LE,skin}}$ or to the upper and lower skin of the trailing edge device $\Delta L_{\text{TE,upperskin}}$ and $\Delta L_{\text{TE,lowerskin}}$.

3.2. Shape Optimization of Morphing Droop Nose for High-Lift Conditions. The optimization procedure described before and shown in Figure 19, coupled with the 3D CST representation introduced in this work, has been applied to the shape design of the morphing droop nose to be installed on the NLF wing optimized in the first part of this paper. The initial design requirements received from the REG-IADP AG2 project include both aerodynamic performance requirements and other general requirements. The novel high-lift devices specifically for the NLF wing shall satisfy the following aerodynamic requirements:

(i) They shall not trigger transition from the laminar to turbulent flow regime on the wing when in retracted position

(ii) They shall provide the following aerodynamic performances:

(a) CL of A/C in takeoff configuration: morphing wing (NLF + morphing) = +2.4%

(b) CL of A/C in landing configuration: morphing wing (NLF + morphing) = +1.7%

The general requirements can be summarized as follows:

(i) Preserve full natural laminar wing

(ii) Allowable skin axial strain: 0 ➔ constant cross-section length (CCL) concept [23]

(iii) Device extension:

(a) Front spar position: 16% local chord

(b) Spanwise configuration: corresponding to the flap extension shown in Figure 12, extendable to preserve shape continuity

(iv) Linear spanwise droop nose deflection: maximum deflection allowed by the constraint on the skin maximum curvature change of 20 (1/m) to avoid normal strain (due to bending) above 1%

(v) Steps & gaps: not allowed on morphing device section and between movable and wing fixed part

Starting from the geometry resulting from the optimization performed on the natural laminar flow (NLF) wing, the morphing shape optimization process was run using two objective functions that try to introduce the maximum droop deflection along the wing span and, at the same time, reduce the drag coefficient Cd in high-lift conditions. This may be suitable for a low-speed condition, corresponding to the landing condition of the Regional Aircraft. This double goal is allowed by the dual loop optimization scheme shown in Figure 19. According to the 3D CST parameterization, only 2 parametric airfoils were identified along the span and included in the set of the most characteristic cross sections: the first one for the inboard region and the second one to interpolate the wing shape between the kink and the section placed at the beginning of the aileron. The parameterized airfoils are represented by a Bernstein polynomial order of $n = 10$ (BPO10), and the droop deflection to be maximized is the equivalent leading edge deflection δ_{LE} introduced in [22]. Each of the 2 inner optimization loops works on 5 implicit variables (A_1 and A_2 for the upper and lower surfaces and c), so that the algorithm is able to work along the 16% of the chord, while the outer aerodynamic loop works only on R_{LE} that is kept fixed on each section in the inner loop. The inner loop can be formulated as follows:

(i) Maximize

$$\frac{1}{2}\sum_{i=1}^{2}\delta_{\text{LE},i} \quad (5)$$

(ii) Such that

$$\begin{aligned} \mathbf{T}_7^T\mathbf{T}_7\mathbf{a}^T &= \mathbf{T}_7^T\mathbf{f}, \\ \Delta\psi_{\text{wing box}} &\equiv (0.16, 1), \\ |\Delta A| &\le 0.2 \cdot A_{\text{u}}, \\ \left|\Delta L_{\text{LE,skin}}\right| &= 0, \\ \max\left(\Delta\kappa(x)\right) &\le 20\frac{1}{m}. \end{aligned} \quad (6)$$

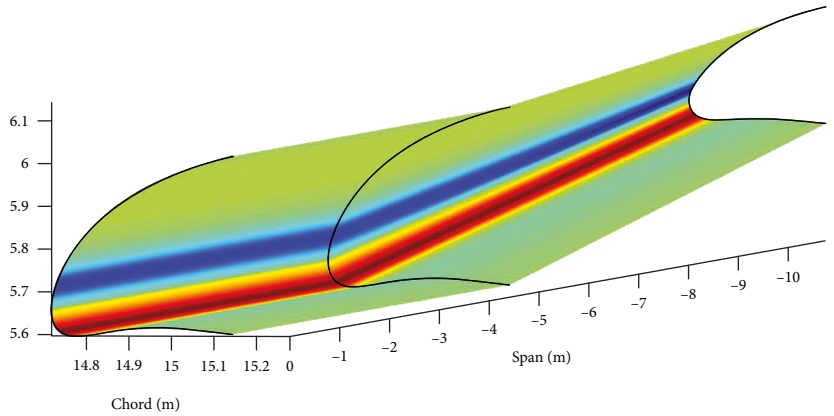

Figure 20: 3D optimal morphing shape and curvature difference.

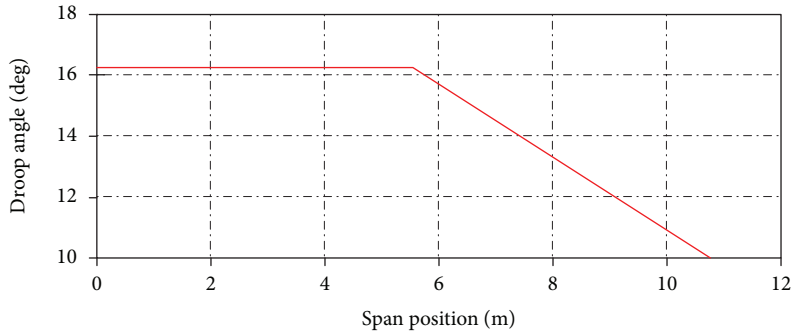

Figure 21: Spanwise droop deflection law of the morphing shape number 3.

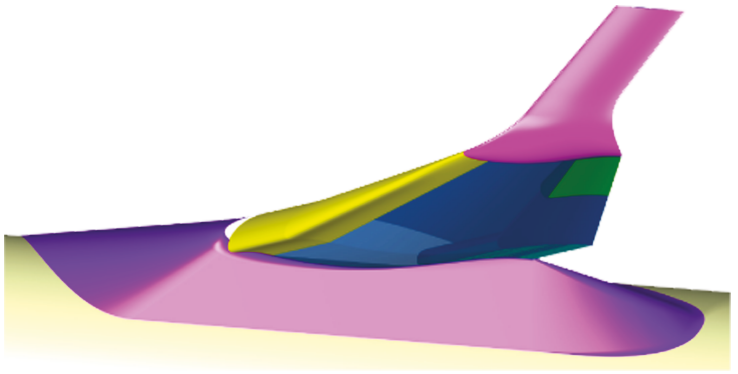

Figure 22: CAD surface of the morphing droop nose.

The first constraint is the wing box volume constraint, evaluated only in the 2D airfoil domain, where T_7 is the *reduced CST–Vandermonde matrix* for the *CST basis* and a contains the extra-coefficients A_1 and A_2, according to the definition of wing box volume constraint provided in [22]. The second constraint defines the undeformed region delimited by the front spar position that is placed at the 16% of the chord. The inflatable term $k_A = 0.2$ limits the airfoil area variation ΔA, with respect to the undeformed one (A_u). According to the initial design requirements, the last two structural consraints are the maximum curvature variation $\Delta\kappa(x)$ and the length variation $\Delta L_{\mathrm{LE,skin}}$ of the morphing leading edge skin, computed with respect to the variable x instead of the nondimensional ψ because they depend on the actual size of the airfoil shape.

The constraints related to the 3D geometry and not included in the inner optimization loop were applied a posteriori acting on the matrix $\mathbf{A}_{m,n}$ where $n = 10$ is the BPO

assigned to the chordwise shape function used for the identification of the parameterized airfoils and $m = 3$ is the BPO selected for the spanwise shape function used to combine the morphing airfoils resulting from the shape optimization and placed at the spanwise boundaries of the morphing region. According to the initial design requirements, the constraint related to the linear deflection law was satisfied by a linear interpolation of the coefficients contained in the first column of the matrix $\mathbf{A}_{m,n}$. The wing box volume constraint was satisfied computing the last 7 column of the matrix $\mathbf{A}_{m,n}$ by least-squares fitting. Figure 20 shows the resulting 3D optimal morphing shape and the corresponding curvature difference that varies between ±20 1/m.

The maximum droop deflection linearly decreases from $\delta_{LE} = 16.2$ deg in the inboard region to $\delta_{LE} = 10.2$ deg at the first section of the aileron, placed at 10.8 m in spanwise, as shown in Figure 21.

According to the initial design requirements, the spanwise configuration is extendable to preserve shape continuity, so it was decided that the deflection gradually vanishes between the section placed at 10.8 m and the wing tip. The CAD model corresponding to the optimal morphing shape and used to generate the mesh for the final aircraft performance assessment is shown in Figure 22.

During the optimization process, the aerodynamic analyses were performed by the MSES solver, which is a fully coupled, implicit code, based on integral boundary layer (IBL) interaction. The flap position was set to 33 deg, while the corresponding flight condition is Mach = 0.197 SL, to take into account the effects of the camber variation introduced by the morphing flap.

3.3. Morphing Droop Nose Definition and 2D Aerodynamic Results. The morphing shape optimization has been performed more than once producing 2 very similar optimal morphing droop noses. The same aerodynamic solver used for the high-fidelity computations performed on the NLF wing was adopted to perform an aerodynamic assessment of these results and select the best one. The droop nose geometries proposed for evaluation, referred as DN02 and DN03, are compared in Figure 23 where the same shape considered for the design of the flaps is shown.

In order to determine the best candidate to be selected for the aircraft, these two droop nose shapes have been adapted to the airfoil and the aerodynamic performance has been evaluated with the flap set at both takeoff and landing positions obtained from 2D optimization. Figure 24 compares the aerodynamic performance obtained for configuration equipped with a droop nose or not. For both, takeoff and landing configurations, a significant increase in stall angle is observed when the droop nose is deflected, leading to an increase in maximum lift value. For the $C_L(\alpha)$ curve, a droop nose acts as a "standard leading-edge device," by extending the baseline $C_L(\alpha)$ curve. For incidences before stall, there is no gain in C_L observed by the use of a droop nose.

This improvement of the stall angle can be explained when considering the pressure distributions at high incidence (Figure 25). Firstly, let us remember that for a high-lift configuration equipped with a flap, a leading edge stall is observed due to the large pressure gradient observed at leading edge. The use of a droop nose device does not affect the flow on the flap and on a large portion of the airfoil. However, a significant decrease in maximum velocity is observed at the airfoil leading edge. As the leading edge stall is driven by the pressure gradient, the use of the droop nose delays the stall onset at a higher incidence.

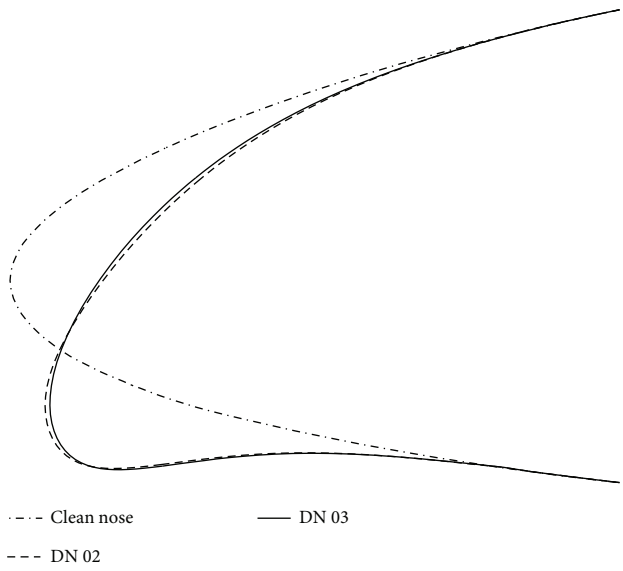

Figure 23: Comparison of droop nose shapes at the wing outboard section.

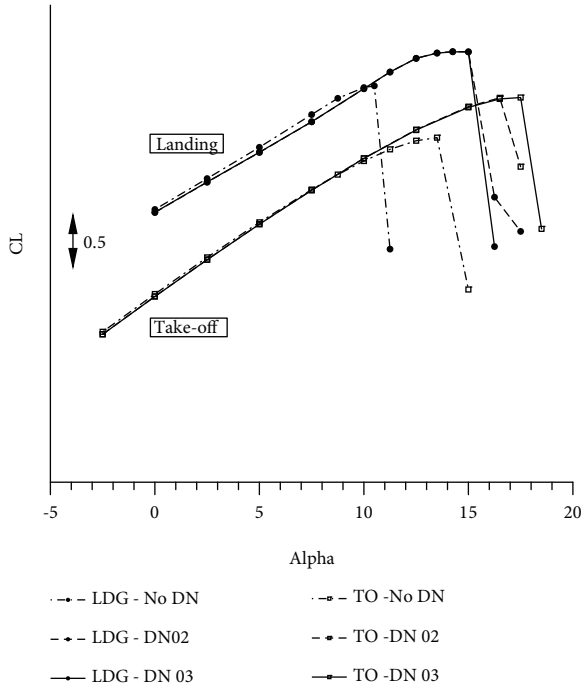

Figure 24: Effect of a droop nose on high-lift computed 2D performance at the outboard wing section.

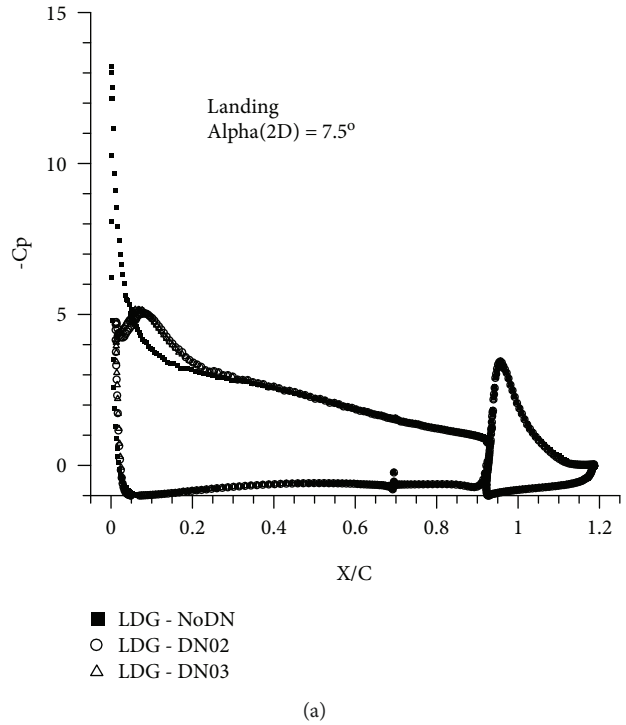

(a)

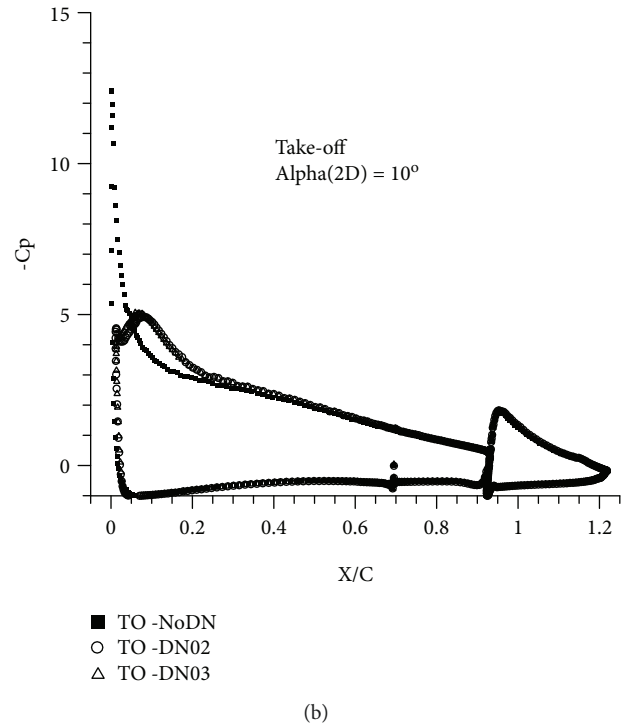

(b)

Figure 25: Effect of a droop nose on computed pressure distributions at the outboard wing section.

About the geometry to be selected, there are no visible effects on global performance in Figure 24. The selection should be done based on local behavior. Figure 26 compares the computed pressure distributions at wing leading edge for the takeoff configuration at $\alpha = 10^{\circ}$. Note that the same conclusions can be obtained if we consider the

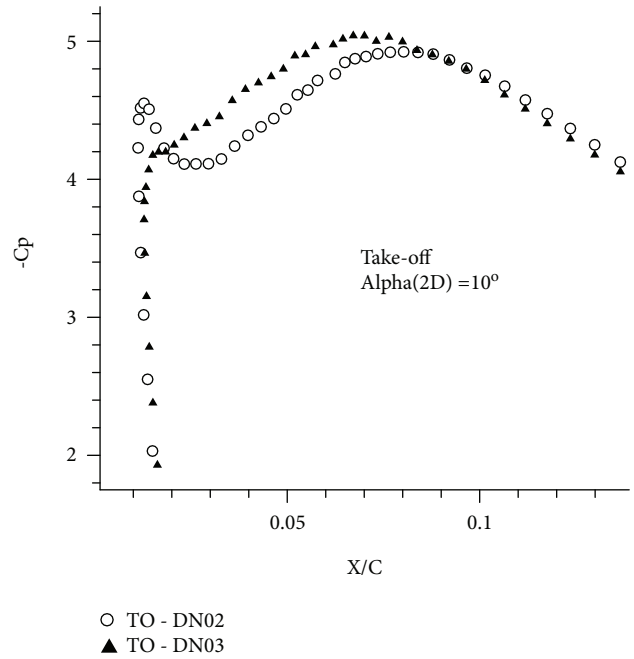

Figure 26: Computed pressure distributions for the two droop nose shapes at high angle of attack. Detail at wing leading edge.

landing configuration, as the droop nose shapes are not modified when moving from takeoff to landing. It can be seen that the pressure distribution developed when using the DN03 shape does not exhibit the small peak that exists with the DN02. The DN03 shape has therefore been selected.

4. Aircraft Performance Assessment in High-Lift Configurations

After the innovative high-lift system is completely defined, the aerodynamic performances are evaluated, at the aircraft level, and the results are used to validate the design procedure presented through the paper. Figure 27 presents the aircraft configurations considered for the performance assessment of the efficiency of the droop nose. It considers the AG2-NLF wing, modified to take into account the flap cove, a 3D flap system at takeoff settings, and a leading edge with the droop nose deflected or not. For the evaluation of the landing configuration, shape morphing was applied to the baseline flap at takeoff settings.

For CFD evaluations, two sets of different background chimera grids have been generated depending on the presence of the droop nose or not. This was necessary in order to consider the detailed geometrical transition between droop nose and unmodified wing shape at wing root. Table 7 gives the number of nodes for each grid.

Three-dimensional computations have been carried out with the elsA software. Firstly, we have to verify how the 2D design compares with the local 3D results obtained at the same location in span. This is done in Figure 28. Though some differences occur, due to local geometrical

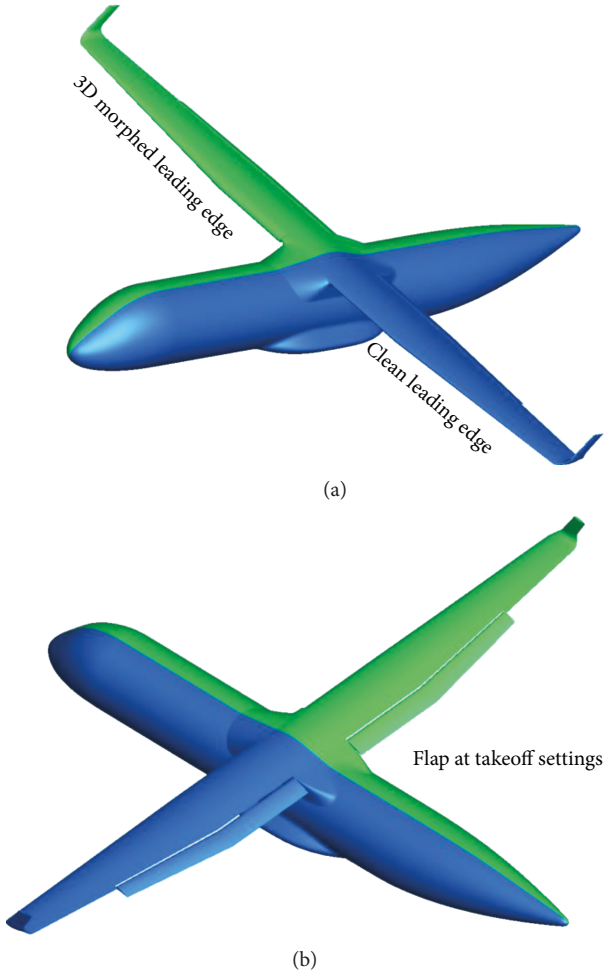

Figure 27: Aircraft configurations considered for the 3D aerodynamic performance assessment.

Table 7: Sizes of the different chimera grids used for 3D CFD performance evaluation.

Background: no droop nose	40,077,177 nodes
Background: with droop nose	72,109,161 nodes
Flaps	3,484,746 nodes

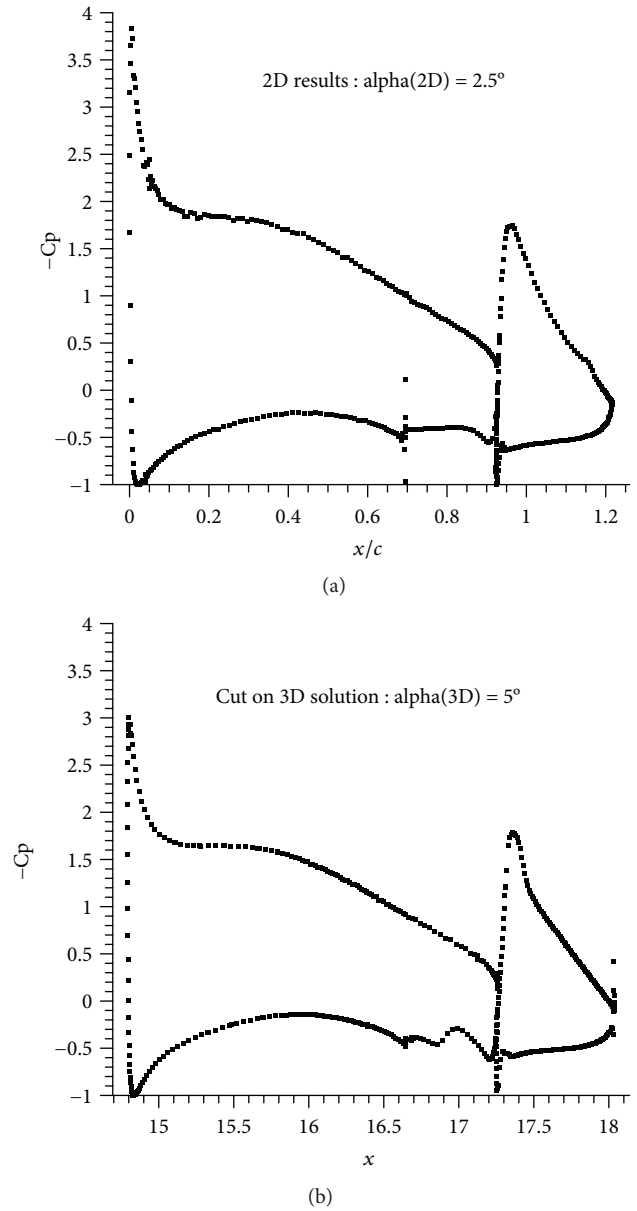

Figure 28: Comparison of Cp distributions between 2D and 3D (no DN – takeoff).

effects (shape, twist) or local 3D aerodynamic effects, there is a general good agreement observed between the two methods, which validate the design methodology used considering local wing sections.

Figure 29 compares the computed $C_L(\alpha)$ for both takeoff and landing configurations, and the $C_L(C_D)$ curves of the takeoff and landing configuration with or without a droop nose device. The effect of the droop nose on the lift curve is similar to the one observed in the 2D work, but with a lower gain in the stall angle for takeoff. Here, an increase of 2.5° is obtained in 3D, instead of 4° in 2D. This can be explained by considering the fact that the wing does not stall at the section that has been considered for the 2D work for takeoff configuration.

For the landing configuration, the use of the morphing droop nose increases the stall angle of about 5°, which is comparable to the gain found in 2D (4.5°), although the flap system is not identical. Additionally, it can be seen that a droop nose seems absolutely necessary for landing conditions for having a maximum lift coefficient that respects the performance required for the AG2-NLF aircraft.

Finally, it can be seen that the use of a morphing droop nose leads to a constant decrease of C_D on the complete C_L range for the takeoff configuration.

These effects on global performance can be understood when comparing the pressure distributions at a given span location of the configurations with and without droop nose (Figure 30 for takeoff, Figure 31 for landing).

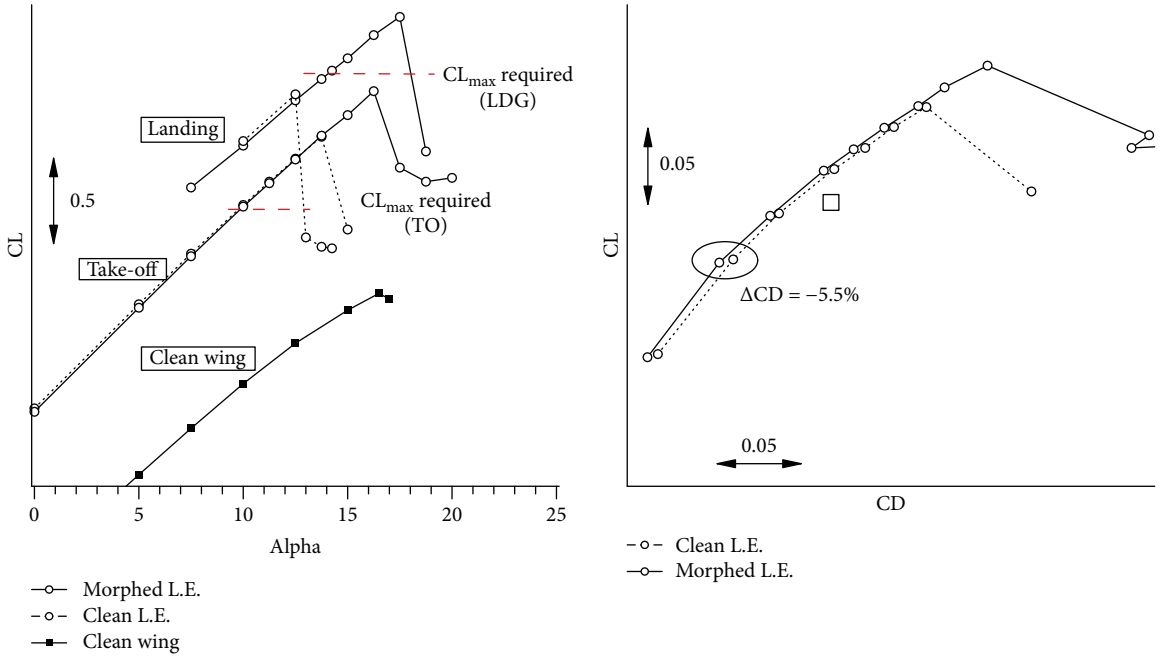

(a) Take-off and landing configurations

(b) Take-off configuration

Figure 29: Effect of a droop nose on the performance in high-lift conditions.

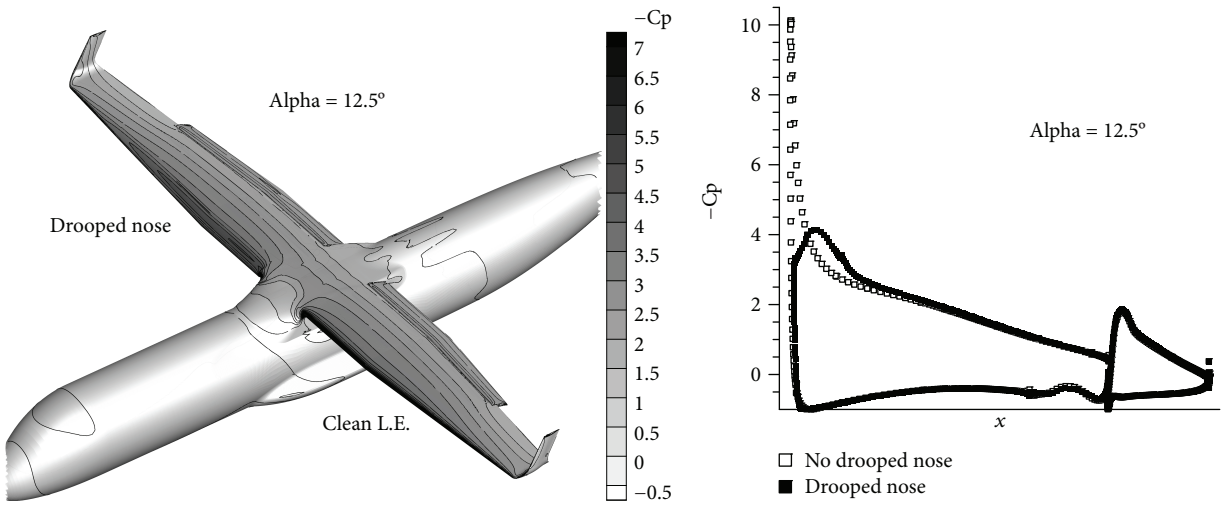

(a)

(b)

Figure 30: Effect of a droop nose on 3D Cp distribution (takeoff, alpha = 12.5°).

(i) Firstly, a strong decrease in pressure peak is observed with the use of a droop nose, as in 2D. This leads to the significant improvement of the stall angle

(ii) Secondly, this strong modification of pressure distribution in the leading edge region also modifies the pressure distribution at wing leading edge, leading to the improvement of C_D for the configuration with droop nose through pressure drag decrease

Finally, the use of the morphing droop nose here proposed modifies the 3D stall process on the wing. Without the droop nose, strong separations occur in the inboard wing close to the junction with the Karman, and near the outboard flap tip (Figure 32(a)). Note that even in that case, the stall onset is not located in the aileron area, as it was requested for the wing design. The use of a droop nose delays the outboard separation, and the stall only occurs at the wing root (Figure 32(b)) at a higher incidence, which is a favorable trend for aircraft design. Similar trends are observed for landing configuration but with higher intensity for the stall with no droop nose (Figure 33), where a leading edge stall on nearly the complete wing is computed.

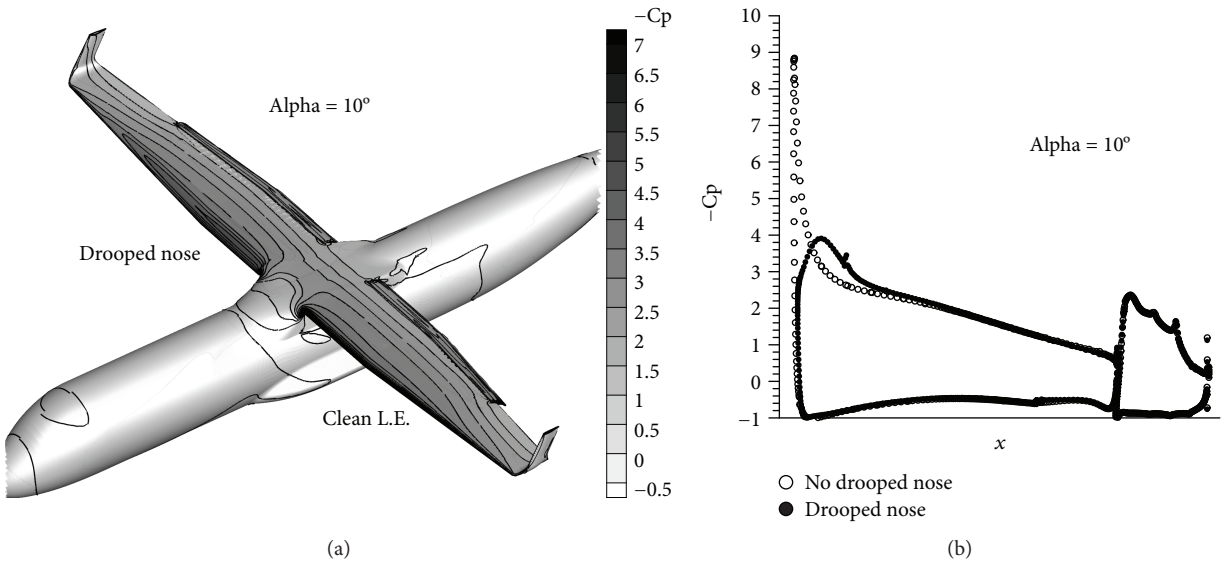

Figure 31: Effect of a droop nose on 3D Cp distribution (landing, alpha = 10.0°).

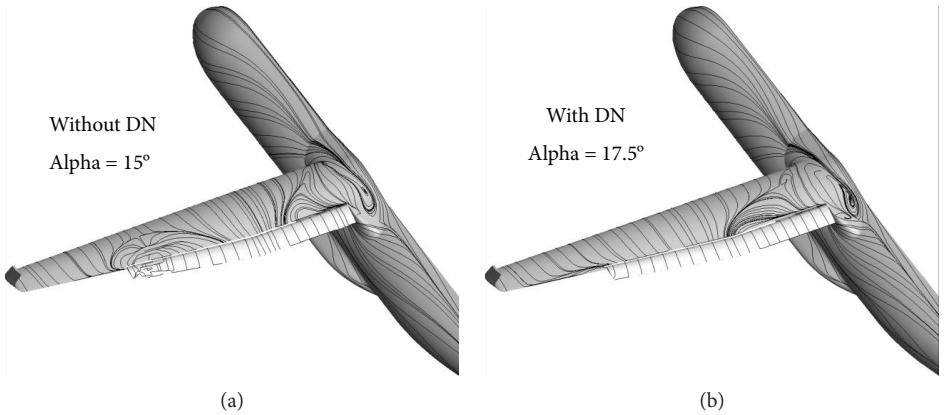

Figure 32: Effect of a droop nose on stall process for takeoff configuration: computed friction lines.

5. Conclusions

The present work describes the approaches and the numerical methodologies developed for the aerodynamic design of a laminar wing of a typical regional aircraft and the high-lift systems to be installed to guarantee the requested high-lift requirements. The initial global requirements, as well as the design and optimization phases of any component, i.e., the laminar wing, the trailing edge flap, and the morphing droop nose, are described in detail. A special emphasis is devoted to the optimization of the morphing droop nose that represents a very challenging design problem since it must combine aerodynamic and structural requirements at the same time. Indeed, the morphing technology here adopted is based on the synergic use of both compliant skin and internal compliant mechanism. Despite that the results reported in this paper are only focused on the aerodynamic design, in case of such as morphing device, the optimal aerodynamic shape must be defined considering the skin structural requirements from the beginning, in compliance with the aerodynamic targets and the materials and manufacturing constraints, so that once actuated is able to match the target shape. The stress distribution along the cover skin of the leading edge is quickly estimated using a simple but effective formula, based on the same geometric representation adopted to introduce the morphing shape changes. Corresponding optimal problem formulation allows considering both aerodynamic objectives and skin structural constraints, and it is considered as a novel element that provides further advantages in this work thanks to the combination with the shape design of the flap, considering that the coupling between the aerodynamic effects of the morphing droop nose and the flap is the only way to catch the actual best performances related to the use of the proposed advanced high-lift device.

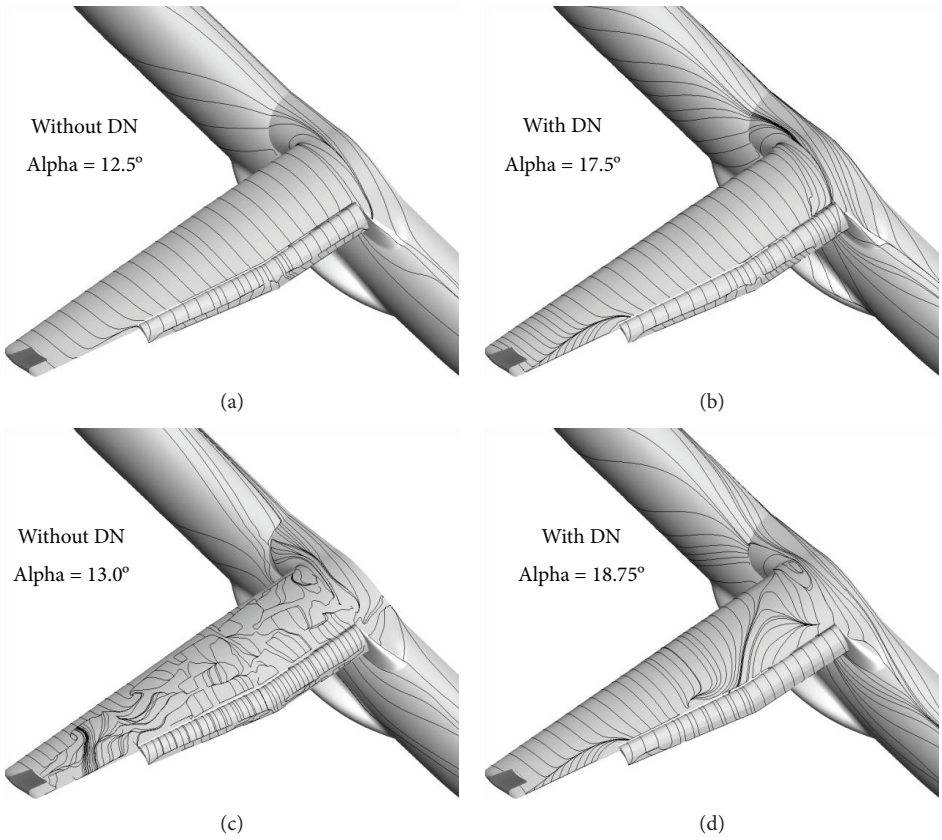

Figure 33: Effect of a droop nose on stall process for landing configuration: computed friction lines.

Table 8: Aerodynamic performance improvements due to the morphing droop nose device.

	$\Delta(C_{Lmax})$	$\Delta(\alpha(C_{Lmax}))$	ΔC_D
Take-off	+10%	+2.5°	-5%
Landing	+15%	+5°	Not relevant

The following results, in terms of aircraft performance, have been obtained:

(i) The use of NLF technology at cruise design point leads to a reduction of 40 drag counts (-16% on C_D) with respect to the turbulent aircraft. It can be noted that some extra gains could be obtained by the optimization of the wing tip device

(ii) It has been observed that the use of a leading edge device is necessary to respect the performance level required for landing conditions. In takeoff conditions, the use of the droop nose increases significantly the stall margin and improves the drag coefficient. Table 8 sums up the performance improvements obtained using the morphing droop nose at low-speed conditions

The procedures adopted demonstrated their validity, and the results obtained meet the initial design requirements. The morphing droop nose guarantees the aerodynamic requirements for the high-lift conditions and, at the same time, the surface smoothness so to preserve the laminar flow in cruise condition when it is not actuated, due to the adopted solution based on a continuous skin.

Data Availability

All the data supporting the results were shown in the paper and can be applicable from the corresponding author.

Conflicts of Interest

The authors declare that there is no conflict of interest regarding the publication of this paper.

Acknowledgments

The AIRGREEN2 Project has received funding from the Clean Sky 2 Joint Undertaking, under the European Union's Horizon 2020 research and innovation programme under grant agreement No. 807089—REG GAM 2018—H2020-IBA-CS2-GAMS-2017. A special thanks goes to Sergio Ricci from Politecnico di Milano, Rosario Pecora from University of Naples "Federico II," and Ignazio Dimino and Salvatore Ameduri from Italian Aerospace Research Centre (CIRA). The studies presented in this article made use of the ONERA-Airbus-Safran elsA software (partially) funded by Airbus, Safran, and ONERA who are co-owners of this software.

References

[1] S. Barbarino, O. Bilgen, R. M. Ajaj, M. I. Friswell, and D. J. Inman, "A review of morphing aircraft," *Journal of Intelligent Material Systems and Structures*, vol. 22, no. 9, pp. 823–877, 2011.

[2] Boeing, Aerospace Company, "Variable camber wing," Second Progress Report, AD911543, 1973.

[3] R. W. de Camp and R. Hardy, "Mission adaptive wing advanced research concepts," in *11th Atmospheric Flight Mechanics Conference, Guidance, Navigation, and Control and Co-located Conferences*, Seattle, WA, USA, August 1984.

[4] K. L. Bonnema and S. B. Smith, "AFTI/F-111 mission adaptive wing flight research program," in *Proceedings of 4th AIAA Flight Test Conference*, pp. 155–161, San Diego, CA, USA, May 1988.

[5] J. Spillman, "The use of variable camber to reduce drag, weight and costs of transport aircraft," *Aeronautical Journal*, vol. 96, pp. 1–9, 1992.

[6] J. W. Smith, W. P. Lock, and G. A. Payne, "Variable camber systems integration and operational performance of the AFTI/F-111 mission adaptive wing," Technical Memorandum, NASA Dryden Flight Research Center, Edwards, CA, USA, 1992.

[7] S. B. Smith and D. W. Nelson, "Determination of the aerodynamic characteristics of the mission adaptive wing," *Journal of Aircraft*, vol. 27, no. 11, pp. 950–958, 1990.

[8] H. P. Monner, T. Bein, H. Hanselka, and E. Breitbach, "Design aspects of the adaptive wing! The elastic trailing edge and the local spoiler bump," Royal Aeronautical Society, Multidisciplinary Design and Optimization, London, UK, 1998.

[9] H. P. Monner, M. Kintscher, T. Lorkowski, and S. Storm, "Design of a smart droop nose as leading edge high lift system for transportation aircrafts," in *50th AIAA/ASME/ASCE/AHS/ASC Structures, Structural Dynamics, and Materials Conference*, p. 10, Palm Springs, CA, USA, May 2009.

[10] V. Lajux and J. Fielding, "Development of a variable camber leading edge device design methodology," in *AIAA 5th ATIO and16th Lighter-Than-Air Sys Tech. and Balloon Systems Conferences*, Arlington, VA, USA, September 2005.

[11] R. Pecora, F. Amoroso, and M. Magnifico, "Toward the bi-modal camber morphing of large aircraft wing flaps: the CleanSky experience," in *Proceedings Volume 9801, Industrial and Commercial Applications of Smart Structures Technologies 2016*, Las Vegas, NV, USA, April 2016.

[12] R. Pecora, F. Amoroso, M. Arena, M. C. Noviello, and F. Rea, "Experimental validation of a true-scale morphing flap for large civil aircraft applications," in *Proceedings Volume 10166, Industrial and Commercial Applications of Smart Structures Technologies 2017*, Portland, OR, USA, April 2017.

[13] I. Dimino, G. Diodati, A. Concilio, A. Volovick, and L. Zivan, "Distributed electromechanical actuation system design for a morphing trailing edge wing," in *Proceedings Volume 9801, Industrial and Commercial Applications of Smart Structures Technologies 2016*, Las Vegas, NV, USA, April 2016.

[14] G. Amendola, I. Dimino, A. Concilio, F. Amoroso, and R. Pecora, "Preliminary design of an adaptive aileron for next generation regional aircraft," *Journal of Theoretical and Applied Mechanics*, vol. 55, pp. 307–313, 2017.

[15] S. Kota, G. Ervin, R. Osborn, and R. A. Ormiston, "Design and fabrication of an adaptive leading edge rotor blade," in *Proceedings of American Helicopter Society 64th Annual Forum*, p. 9, Montreal, Canada, April-May 2008.

[16] S. Kota, R. Osborn, G. Ervin, D. Maric, P. Flick, and D. Paul, "Mission adaptive compliant wing-design, fabrication and flight test," in *RTO Applied Vehicle Technology Panel (AVT) Symposium*, RTO-MP-AVT-168, Evora, Portugal, 2009.

[17] A. De Gaspari and S. Ricci, "Application of the active camber morphing concept based on compliant structures to a regional aircraft," in *Proceedings Volume 9059, Industrial and Commercial Applications of Smart Structures Technologies 2014*, pp. 1–21, San Diego, CA, USA, March 2014.

[18] A. De Gaspari, L. Riccobene, and S. Ricci, "Design, manufacturing and wind tunnel validation of a morphing compliant wing," *Journal of Aircraft*, vol. 55, no. 6, pp. 2313–2326, 2018.

[19] A. De Gaspari, A. Gilardelli, S. Ricci, A. Airoldi, and F. Moens, "Design of a leading edge morphing based on compliant structures in the framework of the CS2-AirGreen2 project," in *ASME 2018 Conference on Smart Materials, Adaptive Structures and Intelligent Systems (SMASIS 2018), Volume 1: Integrated System Design and Implementation*, pp. 1–9, San Antonio, TX, USA, September 2018.

[20] A. De Gaspari, A. Gilardelli, S. Ricci, A. Airoldi, and F. Moens, "Design of a leading edge morphing based on compliant structures for a twin-prop regional aircraft," in *2018 AIAA/AHS Adaptive Structures Conference, AIAA SciTech Forum*, pp. 1–19, Kissimmee, FL, USA, January 2018.

[21] H. Sobieczky, "Parametric airfoil and wings," in *Recent Development of Aerodynamic Design Methodologies. Notes on Numerical Fluid Mechanics (NNFM), vol 65*, K. Fujii and G. S. Dulikravich, Eds., pp. 71–88, Vieweg+Teubner Verlag, 1998.

[22] A. De Gaspari and S. Ricci, "Knowledge–based shape optimization of morphing wing for more efficient aircraft," *International Journal of Aerospace Engineering*, vol. 2015, Article ID 325724, 19 pages, 2015.

[23] A. De Gaspari and S. Ricci, "A two–level approach for the optimal design of morphing wings based on compliant structures," *Journal of Intelligent Material Systems and Structures*, vol. 22, no. 10, pp. 1091–1111, 2011.

[24] G. N. Vanderplaats, *DOT-Design Optimisation Tools Program*, Vanderplaats Research and Development, Colorado Springs, CO, USA, 1995.

[25] M. Drela and M. B. Giles, "Viscous-inviscid analysis of transonic and low Reynolds number airfoils," *AIAA Journal*, vol. 25, no. 10, pp. 1347–1355, 1987.

[26] F. Moens and C. Wervaecke, "Multi-point optimization of shapes and settings of high-lift system by means of evolutionary algorithm and Navier-Stokes equations," *Engineering Computations*, vol. 30, no. 4, pp. 601–622, 2013.

[27] L. Cambier, S. Heib, and S. Plot, "The Onera *elsA* CFD software: input from research and feedback from industry," *Mechanics & Industry*, vol. 14, no. 3, pp. 159–174, 2013.

[28] J. Reneaux, P. Beaumier, and P. Giroudroux-Lavigne, "Advanced aerodynamic applications with the elsA software," *AerospaceLab*, vol. 2, pp. 1–21, 2011, http://www.aerospacelab-journal.org.

[29] A. Jameson, W. Schmidt, and E. Turkel, "Numerical solution of the Euler equations by finite volume methods using Runge

Kutta time stepping schemes," in *14th Fluid and Plasma Dynamics Conference, Fluid Dynamics and Co-located Conferences*, pp. 81–1259, Palo Alto, CA, USA, June 1981.

[30] P. R. Spalart, "Strategies for turbulence modelling and simulations," *International Journal of Heat and Fluid Flow*, vol. 21, no. 3, pp. 252–263, 2000.

[31] F. R. Menter, "Two-equation eddy-viscosity turbulence models for engineering applications," *AIAA Journal*, vol. 32, no. 8, pp. 1598–1605, 1994.

[32] R. Houdeville, P. Bardoux, and V. Moreux, "3D boundary layer computations on Wing-Pylon-Nacelle configuration," in *Workshop on Aspects of Airframe Engine Integration for transport Aircraft*, Braunschweig, Germany, March 1996.

[33] G. Casalis and D. Arnal, "ELFIN II, sub-task 2.3: data base method. Development and validation of the simplified method for pure crossflow instability at low speed," ELFIN II-European Laminar Flow Investigation, Technical Report, 1996.

[34] F. Moens, J. Perraud, A. Krumbein, T. Toulorge, P. Iannelli, and A. Hanifi, "Transition prediction and impact on 3D high-lift wing configuration," in *25th AIAA Applied Aerodynamics Conference, Fluid Dynamics and Co-located Conferences*, pp. 25–28, Miami FL, USA, June 2007.

[35] Introduction to ANSYS ICEM CFD HEXA, Ansys, Inc, http://www.ansys.com/Services/training-center/platform/introduction-to-ansys-icem-cfd-Hexa.

[36] C. Benoit, S. Peron, and S. Landier, "Cassiopee: a CFD pre- and post-processing tool," *Aerospace Science and Technology*, vol. 45, pp. 272–283, 2015.

[37] B. M. Kulfan, "Universal parametric geometry representation method," *Journal of Aircraft*, vol. 45, no. 1, pp. 142–158, 2008.